Dalton Transactions

ROYAL SOCIETY OF CHEMISTRY

PAPER

Check for updates

Cite this: *Dalton Trans.*, 2024, **53**, 171

Observation of inserted oxocarbonyl species in the tantalum cation-mediated activation of carbon dioxide dictated by two-state reactivity†

Jia Han,[a] Pengcheng Liu,[b,c] Binglin Qiu,[a] Guanjun Wang, *[d] Shilin Liu [a] and Xiaoguo Zhou *[a]

Received 27th October 2023,
Accepted 16th November 2023

DOI: 10.1039/d3dt03593j

rsc.li/dalton

Reductive activation of carbon dioxide (CO_2) has drawn increasing attention as an effective and convenient method to unlock this stable molecule, especially *via* transition metal-catalyzed reactions. Taking the $[TaC_4O_8]^+$ ion–molecule complex formed in the laser ablation source as a representative, the reactivity of the tantalum metal cation towards CO_2 molecules is explored using infrared photodissociation spectroscopy combined with quantum chemical calculations. The strong absorption in the carbonyl stretching region provides solid evidence for the insertion reactions into C=O bonds by the tantalum cation. Two inserted oxocarbonyl products are identified based on the great agreement between the experimental results and simulated infrared spectra of energetically low-lying structures in the singlet and triplet states. The pivotal role of two-state reactivity in driving CO_2 activation among three different spin states is rationalized by potential energy surface analysis. Our conclusion provides valuable insight into the intrinsic mechanisms of CO_2 activation by the tantalum metal cation, highlighting the affinity of tantalum for C=O bond insertion in addition to typical "end-on" binding configurations.

Introduction

The ubiquitous simple triatomic molecule carbon dioxide (CO_2) serves as a potent building block with huge potential for use in the chemical industry, despite being consistently blamed for global warming. Nevertheless, its intrinsic thermodynamic stability and kinetic inertness make it very difficult and challenging to convert CO_2 into more valuable products. Not surprisingly, sheer endless endeavors have been made to explore the catalytic conversion of CO_2 molecules into active species through fixation and at least partially bond-weakening to further enable practical applications.[1–6]

Inspired by heterogeneous catalysis involving incompletely coordinated metal centers on supported surfaces or frameworks, studies on transition metal atoms and ions as well as associated metal oxides with CO_2 have received wide attention as prototypical model systems.[1,7–11] The related ion–molecule reactions in the gas phase are perceived as an outstanding model for investigating the elementary steps of catalytic reactions, free from perturbing effects in the surroundings such as solvents and counterions.[12,13] Infrared photodissociation spectroscopy has been widely applied to gain detailed insights into the binding behavior and mutual interactions between metal catalysts and CO_2 molecules, providing a sensitive probe for geometric characteristics as any structural rearrangements will be encoded in the vibrational spectra.[14–18] Apart from experimental investigations, there are also a considerable amount of theoretical studies focusing on transition metal-mediated reactions with CO_2 in an effort to elucidate salient features of mechanisms and kinetics.[19–23]

Taking the electronic structure of CO_2 into consideration, the most commonly adopted method of effective activation concerns electron density donation to the antibonding π^* orbital, leading to a negatively charged CO_2 moiety and further enabling overall reduction of bond strength along with bending distortion from its initial linear geometry.[2] The changes in the charge distribution and geometric structures give rise to vibrational frequency shifts regarding the asymmetric stretching mode of the CO_2 molecule. Weber and coworkers probed significantly red-shifted vibrational frequencies marked by several hundred wavenumbers relative to the

[a]*Hefei National Laboratory for Physical Sciences at the Microscale, Department of Chemical Physics, University of Science and Technology of China, Hefei 230026, China. E-mail: xzhou@ustc.edu.cn*
[b]*Anhui Institute of Optics and Fine Mechanics, Hefei Institutes of Physical Science, Chinese Academy of Sciences, Hefei 230031, China*
[c]*Science Island Branch, Graduate School, University of Science and Technology of China, Hefei 230026, China*
[d]*Department of Chemistry, Fudan University, Shanghai 200433, China. E-mail: gjwang@fudan.edu.cn*

† Electronic supplementary information (ESI) available. See DOI: https://doi.org/10.1039/d3dt03593j

free CO_2 asymmetric stretch in the case of anionic $[M(CO_2)_n]^-$ clusters (M = Ti, Au, Ag, *etc.*), offering detailed exploration of the function of electron-rich CO_2 reduction catalysts.[24–30]

In contrast to anionic analogues, spectroscopic investigations on cationic metal–CO_2 complexes have found little evidence for direct activation, while a similar pattern specified by weak blue shifts of the CO_2 asymmetric stretching mode has been observed.[31–36] The charge–quadrupole interaction has been revealed to play a leading role in determining the binding motifs between the metal center and CO_2 ligands, which brings about almost exclusively monodentate coordination to the metal ion *via* one of the oxygen atoms from CO_2. As the number of ligands increases, weakly bound CO_2 molecules start to form the second solvent shell and the corresponding asymmetric stretching frequencies appear in the spectral region close to that of isolated CO_2. In a thorough survey of the chemistry between 46 metal cations and CO_2 at room temperature, nine early transition metals were found to be capable of activating CO_2 through oxygen-atom abstraction in a bimolecular fashion.[8] The formation of metal–carbonyl complexes involving insertion reactions has been detected in the infrared studies of Ti^+, V^+ and Ni^+ cations interacting with different numbers of CO_2 molecules.[34,35,37] This reduction constitutes a critical step in the catalytic hydrogenation of CO_2 and the resulting CO is an important feedstock in the industrial synthesis of chemical fuels. In addition to the dissociative reduction, a novel M[η^2-(C,O)O] binding motif with the formation of a bent CO_2^- moiety was determined in the $[V(CO_2)_7]^+$ complex, indicative of the ligand-induced activation by the vanadium cation.[10]

Here, we describe the reactivity of the cationic tantalum transition metal atom towards CO_2 molecules in the gas phase using infrared photodissociation spectroscopy combined with quantum chemical calculations. In the cationic complex $[TaC_4O_8]^+$, intracluster reactions are expected in light of the ability of early transition metals to adopt different spin and oxidation states. The comparison of the experimental spectrum with computational results allows for complementary determination of various structural motifs, including C═O bond insertion products and end-on configurations. Microscopic reaction mechanisms for the activation of the CO_2 molecule by the tantalum cation are also discussed at the molecular level. This result provides instructive clues to design novel catalysts involving transition metal complexes for the chemical conversion of CO_2.

Methods

Infrared photodissociation spectroscopy

The infrared photodissociation spectrum of the tantalum cation complexed with CO_2 molecules was measured using a collinear tandem time-of-flight mass spectrometer coupled with a laser vaporization supersonic cluster source. The experimental instrument has been described in detail previously.[38,39] The 1064 nm fundamental of a Nd:YAG laser (Continuum, Minilite II; 10 Hz repetition rate and 6 ns pulse width) was used to vaporize a rotating tantalum metal target. Cation complexes were produced by laser ablation in expansion of helium gas seeded with 2% CO_2 using a pulse valve (General Valve, Series 9) at a stagnation pressure of 1.0–1.2 × 10^6 Pa. After free expansion, the produced cation complexes were skimmed and analyzed using a typical Wiley-McLaren time-of-flight mass spectrometer. The ions of interest were mass-selected and decelerated into the extraction region of a second collinear time-of-flight mass spectrometer, where they were intersected by a tunable IR laser. The fragment and parent ions were reaccelerated and mass-analyzed using a second time-of-flight mass spectrometer equipped with a dual micro-channel plate (MCP) detector.

The infrared photodissociation spectrum was obtained by monitoring the fragmentation yield as a function of the dissociation IR laser wavelength and then normalizing to the parent ion signal. Typical spectra were recorded by scanning the infrared laser in steps of 2 cm^{-1} and averaging over 300 laser shots at each wavelength. The tunable IR laser source used in this study was generated using a KTP/KTA optical parametric oscillator/amplifier system (OPO/OPA, Laser Vision) pumped with a Nd:YAG laser (Continuum, Powerlite 8000). The laser photon energy was 1.0–2.0 mJ per pulse in the region of 2000–2500 cm^{-1}. The infrared laser wavenumber was calibrated with a commercial wavemeter (Coherent, Wave-Master) using the well-known absorptions of CO. The IR beam propagation path was purged with nitrogen to minimize air absorption.

DFT calculations

Quantum chemical calculations were performed to determine molecular structures and to validate vibrational assignments. Considering there might be various isomers at the same mass-to-charge ratio, a large number of initial complex geometries were generated randomly using Genmer.[40] Preliminary screening was performed with the semiempirical quantum mechanical method GFN2-xTB,[41] using the xtb[42] program through Moclus.[40,43] The pre-optimized configurations were classified and sorted in energy. Further optimization and harmonic vibrational frequency calculation of low-lying structures were carried out with the PBE0-D3(BJ) functional in combination with the def2-TZVP basis set.[44–46] Harmonic vibrational frequencies were scaled and further convoluted with Lorentzian functions using 8 cm^{-1} full width at half-maximum (FWHM) to simulate the infrared spectra of energetically low-lying complexes. Intrinsic reaction coordinate (IRC) calculations were performed to confirm that all of the reported transition states link the corresponding reactants and products.[47–50] All the DFT calculations were carried out with the Gaussian 16 software package.[51]

Results and discussion

Determination of the cationic core in the $[TaC_4O_8]^+$ cation complex

The oxygen-atom abstraction reaction (R1) between the highly reactive Ta^+ metal cation and CO_2 was reported to occur

efficiently at the collision rate by Wesendrup and Schwarz.[52] In addition, the subsequent reaction (R2) to form the dioxo-cation TaO_2^+ from TaO^+ was examined at the PBE0-D3(BJ)/def2-TZVP level of theory. The enthalpy changes of these two exothermic reactions were calculated to be −31.9 kcal mol^{-1} for (R1) and −3.1 kcal mol^{-1} for (R2), respectively. As a result, TaO^+ and TaO_2^+ as the oxygen transfer reaction products could be cation cores to bind successive CO_2 ligands, as well as the Ta^+ cation itself under real experimental conditions. In order to evaluate the contribution of each possible isomeric configuration from a thermodynamics view, it is necessary to conduct a global screening of stable candidates for the $[TaC_4O_8]^+$ cation complex, commencing with the examination of tantalum metal oxides coordinated with CO and CO_2 ligands.

$$Ta^+ + CO_2 \rightarrow TaO^+ + CO \quad (R1)$$

$$TaO^+ + CO_2 \rightarrow TaO_2^+ + CO \quad (R2)$$

The ground electronic states of the Ta^+, TaO^+ and TaO_2^+ cations have been found to be different, *i.e.* quintet for Ta^+, triplet for TaO^+ and singlet for TaO_2^+.[53,54] Accordingly, instead of complying with the spin conservation scenario where the reactants, transition states and products remain on a uniform spin surface, the oxygen abstraction reaction may proceed on potential energy surfaces with different spin multiplicities, suggesting that a spin conversion process occurs in the laser ablation source. After extensive exploration, the most favorable reaction pathways for the oxygen-atom abstraction on the singlet, triplet and quintet energy surfaces, together with relevant intermediate structures, are illustrated in Fig. 1.

Previous studies have shown that products in a laser vaporization source are dominantly populated in the ground state probably due to sufficient collisions in the molecular beam, albeit with a high-temperature environment resulting from laser ablation.[55–58] Thus, the Ta^+ cation in the quintet state (the ground state) is certainly the most predominant reagent under experimental conditions. Starting from the stable encounter complex ($^5[Ta]^+\cdots OCO$), Ta^+ cation insertion into the C═O bond initially proceeds along the quintet pathway (Fig. 1a). Although the thermal energy of this complex formed in the laser ablation source may be sufficient to overcome the transition state in the quintet spin state which lies 19.8 kcal mol^{-1} above the reactants, a spin crossover from the quintet to triplet state *via* a crossing point is preferred due to the corresponding rather low energy barrier (24.4 kcal mol^{-1} for the triplet state *versus* 41.6 kcal mol^{-1} for the quintet state). In this manner, reaction (R1) is more likely to take place by surmounting the triplet transition state which is higher in energy by only 2.6 kcal mol^{-1} relative to the initial reactants $^5[Ta]^+$ and CO_2. The newly formed CO ligand tends to remain bound to the metal center and subsequently produces the inserted oxocarbonyl species $^3[OTa^+CO]$ along reaction coordinates.

An examination of the reaction surfaces for the next bond activation step is depicted in Fig. 1b. The second oxygen-atom abstraction (R2) either remains on the triplet spin state surface the same as products in (R1), or occurs *via* spin inversion from the triplet to the singlet surface as the low-spin encounter complex lies below the triplet counterpart by 7.1 kcal mol^{-1}. The latter route is not only energetically favored, but also avoids the significantly less stable triplet transition state, while the singlet one pulls down 38.9 kcal mol^{-1} in energy and can directly convert to oxocarbonyl products without any substantial energy barrier. For the quintet spin surface, however, this process is hindered by the high entrance channel, which is located well above the triplet and singlet states and is therefore cannot be accessed under ambient conditions.

From a mechanistic point of view, the computationally determined reaction scenario for the sequential activation of CO_2 requires explanations involving a reaction surface that tra-

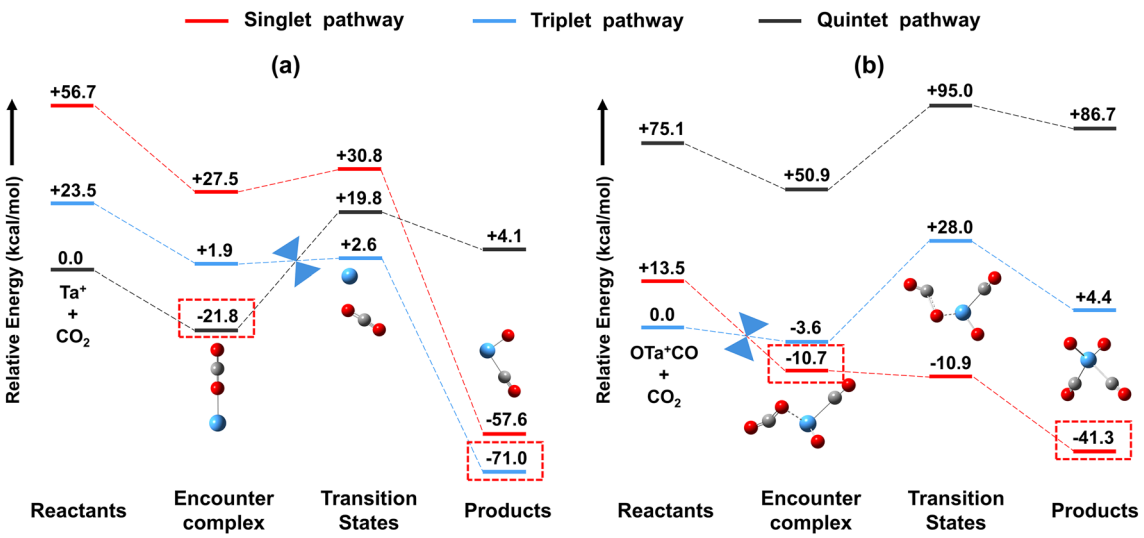

Fig. 1 Reaction pathways for the oxygen-atom abstraction on the singlet, triplet and quintet energy surfaces of reaction R1(a) and R2(b) calculated at the PBE0-D3(BJ)/def2-TZVP level of theory, where the relative energies are in kcal mol^{-1}. The dominant cation complexes are marked with boxes.

verses three different spin states. This type of spin-crossing phenomenon is termed two-state reactivity (TSR) and has been employed to help understand complex reactions on different landscapes brought about by the accessibility of multiple spin states in organometallic chemistry.[59–64] In particular, the TSR scenario has been proposed as a fundamental theory to interpret reaction mechanisms involving transition-metal compounds.[21,65–69] Our calculation confirms that spin crossover plays a critical role in facilitating the C═O bond cleavage of CO_2 molecules by the tantalum cation. Based on the above analysis, the inserted products $[TaO_2(CO)_2(CO_2)_2]^+$ and $[TaO(CO)(CO_2)_3]^+$, together with the end-on complex $[Ta(CO_2)_4]^+$, all could be isomeric forms of the $[TaC_4O_8]^+$ cation complex observed in experiments.

Structures and simulated infrared spectra of isomers for the $[TaC_4O_8]^+$ cation complex

When taking $[TaO_2]$ as the center, only the singlet electronic state was taken into account, given its consistently lower energy than the triplet and quintet analogues. Four low-lying isomers of the $[TaO_2(CO)_2(CO_2)_2]^+$ cation complex and the corresponding simulated infrared spectra are shown in Fig. 2, with detailed geometric parameters listed in Fig. S1.† In the most stable isomer IDa, two CO and CO_2 ligands are alternately distributed on either side of the central ion. The coordination bond lengths are calculated to be 2.29 and 2.63 Å for Ta···CO, while 2.23 and 2.47 Å for Ta···OCO, respectively. Such large distances imply noncovalent interactions between the metal ion and ligands, which is substantiated by the predicted stretching vibrational frequencies of two CO moieties at 2325 and 2335 cm^{-1} close to that of the free CO stretching vibration at 2241 cm^{-1} derived from calculations. This blue shift can be explained by negligible M → CO π back-donation originating from the high-valence oxidation state of the metal as demonstrated in "non-classical" transition metal carbonyls.[70–75] Moreover, the out-of-phase combination of asymmetric stretching motions of two CO_2 ligands is calculated to be 2466 cm^{-1}, while the in-phase asymmetric stretching combination has a vibrational frequency of 2489 cm^{-1} with weaker intensity.

The second lowest-energy isomer IDb, which is higher in energy than IDa by 4.2 kcal mol^{-1} (Table 1), exhibits a nearly linear binding mode with the Ta···CO distances of 2.33 and 2.35 Å, respectively. Two CO stretching modes present a primary peak at 2344 cm^{-1} and a shoulder at 2353 cm^{-1}. In the CO_2 asymmetric stretching frequency range, two peaks are predicted at 2457 and 2488 cm^{-1}, while their relative intensities exhibit an opposite trend to that of IDa. The third candidate, IDc, has the C_{2v} symmetry and lies above the global minimum IDa by 5.6 kcal mol^{-1}. The bond lengths of Ta···CO and Ta···OCO are calculated to be 2.47 Å and 2.22 Å, respectively. Accordingly, a virtually degenerate peak at 2321 cm^{-1} in the CO stretching frequency range and two CO_2 asymmetric stretching absorptions (2479 and 2491 cm^{-1}) with a small band gap are predicted. In the fourth isomer with a C_s symmetry, IDd, CO and CO_2 ligands are separately distributed on either side of the TaO_2 center. The bonding distances between the Ta atom and two CO_2 ligands are 2.22 and 2.35 Å, while only one CO binds closely to the center (2.31 Å). The last carbonyl group attaches to the Ta atom with a significantly larger distance of 3.78 Å, leading to two well-separated carbonyl stretching peaks at 2267 and 2345 cm^{-1}.

With [TaO] as the center core, a large number of $[TaO(CO)(CO_2)_3]^+$ structures at the singlet and triplet states were scruti-

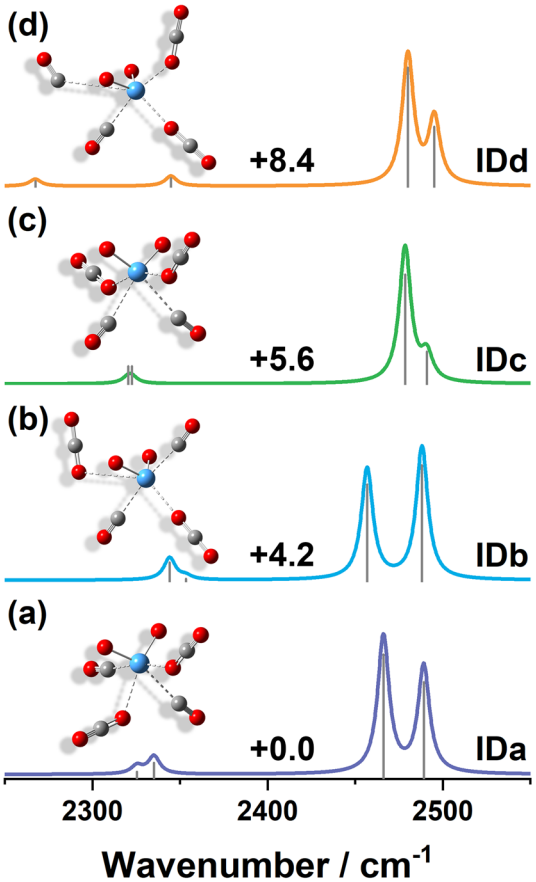

Fig. 2 Simulated vibrational spectra of low-lying isomers for the $[TaO_2(CO)_2(CO_2)_2]^+$ cation complex in the region of 2250–2550 cm^{-1} derived from calculated harmonic frequencies and intensities at the PBE0-D3(BJ)/def2-TZVP theory level. Relative energies are given in kcal mol^{-1}.

Table 1 Calculated relative energies (kcal mol^{-1}) of low-lying isomers in different spin states for the $[TaC_4O_8]^+$ cation complex at the PBE0-D3(BJ)/def2-TZVP level of theory

Formula	Spin state	Isomer	Relative energy (kcal mol^{-1})
$[TaO_2(CO)_2(CO_2)_2]^+$	Singlet	IDa	0.0
	Singlet	IDb	4.2
	Singlet	IDc	5.6
	Singlet	IDd	8.4
$[TaO(CO)(CO_2)_3]^+$	Singlet	IMa	0.0
	Triplet	IMb	8.9
	Triplet	IMc	9.1
$[Ta(CO_2)_4]^+$	Quintet	INa	0.0

nized for viable candidates. It is worth noting that the global minimum is still in the singlet state rather than being consistent with the triplet ground electronic term of TaO^+. Below the energy limit of 10 kcal mol^{-1}, three isomers are included in the following discussion, *i.e.* IMa (singlet), IMb (triplet) and IMc (triplet) and their detailed geometric parameters are available in the ESI (Fig. S2†). The geometric structures and the corresponding simulated infrared spectra are shown in Fig. 3. In isomer IMa with a C_s symmetry, three CO_2 ligands directly connect to the Ta atom in an η^1-O mode. The Ta···CO distance of 2.04 Å is shorter than that in isomer IDa with the CO stretching frequency red-shifted to 2087 cm^{-1}. It is evident from the comparison between the [TaO] and [TaO_2] cases that a lower degree of oxidation of the metal center leads to an enhanced π back-donation effect from filled d orbitals of the metal. Due to its symmetric geometry, IMa exhibits coupled CO_2 oscillators, *i.e.*, the out-of-phase combination of asymmetric stretching modes of two equivalent CO_2 ligands at 2475 cm^{-1} and the out-of-phase combination of three CO_2 stretching modes at 2478 cm^{-1}. These frequencies are too close to be discerned, producing a prominent peak centered at 2476 cm^{-1} after broadening. A weak peak at 2501 cm^{-1} is also predicted for IMa, which originates from the in-phase combination of three CO_2 asymmetric stretching modes. The second low-lying singlet isomer lies 12.3 kcal mol^{-1} above IMa where one CO_2 ligand binds to Ta in a bidentate η^2-(C,O) fashion (see details in the ESI†) and is therefore not taken into consideration given its significantly higher energy.

The two isomers IMb and IMc in the triplet state are higher in energy than IMa by 8.9 and 9.1 kcal mol^{-1}, respectively. Both of them have three monodentate CO_2 ligands and an inserted OTaCO unit with a C_s symmetry, in which the σ plane is located on the O–Ta–CO plane. Similar to IMa, shorter Ta···CO distances of 2.11 Å in IMb and 2.16 Å in IMc are predicted, as well as substantially red-shifted CO stretching frequencies, *e.g.* 2062 cm^{-1} for IMb and 2197 cm^{-1} for IMc (out of the frequency range in Fig. 3). The calculated infrared spectrum of IMb in the CO_2 asymmetric stretch region is nearly identical to that of IMa, albeit with a much weaker peak at 2496 cm^{-1}. Isomer IMc shows a prominent band at 2466 cm^{-1} and a small feature at 2490 cm^{-1}. Additionally, isomers in the quintet state have too higher energy and are excluded from spectral assignments, even though including a special structure with a carbonato moiety (Fig. S2e†). Based on the calculated reaction pathway for the second oxygen atom abstraction on the singlet energy surface shown in Fig. 1b, the formed singlet [TaO] core will easily convert to the singlet [TaO_2] with no energy barrier, resulting in a population of the [TaO(CO)$(CO_2)_3$]$^+$ complex dominated by the triplet species. Consequently, IMb in the triplet state instead of the singlet IMa is the most probable cation core for the [TaO(CO)$(CO_2)_3$]$^+$ complex in experiments.

CO_2 ligands in metal–CO_2 cationic complexes are usually categorized as part of the core structure or external solvent.[9] The former is characterized by covalent binding motifs with the metal ion, while the latter acts as a solvent weakly bound to the cation core. Following this viewpoint, the pure solvation of Ta^+ by CO_2 molecules may also come into play in the [TaC_4O_8]$^+$ complex. In order to examine this possibility, all three spin states were checked in the course of locating minima for the [Ta$(CO_2)_4$]$^+$ complex and the corresponding geometric parameters are listed in Fig. S3.† Notably, four-coordinated structures turn out to be the lowest-energy ones among all obtained geometries for different spin multiplicities. When the energy limit of 10 kcal mol^{-1} was applied, only the most stable isomer INa in the quintet state stands out and the simulated infrared spectrum is plotted in Fig. 4. INa is a highly symmetric structure with a planar D_{4h} symmetry where the Ta···OCO distance is 2.23 Å, leading to only one IR-active vibrational mode at 2476 cm^{-1} derived from the out-of-phase combinations of the CO_2 asymmetric stretch. The strong charge–quadrupole electrostatic interaction between Ta^+ and CO_2 molecules causes its apparently blue-shifted feature relative to the free CO_2 asymmetric stretch.

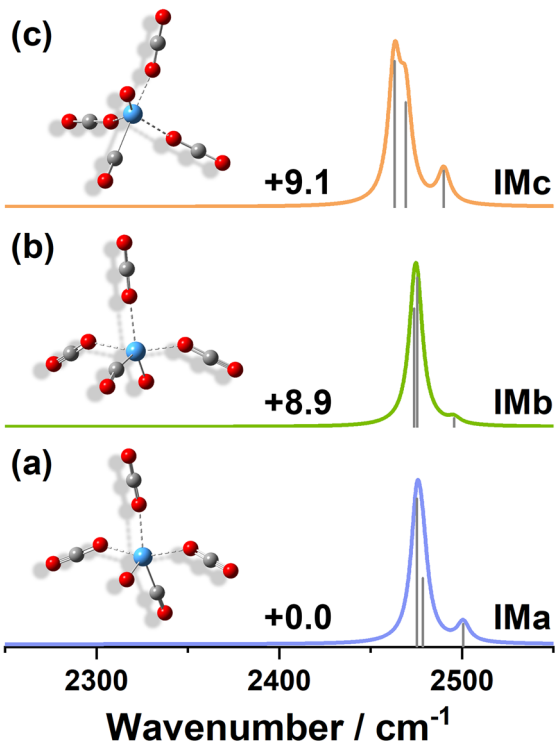

Fig. 3 Simulated vibrational spectra of low-lying isomers for the [TaO(CO)$(CO_2)_3$]$^+$ cation complex in the region of 2250–2550 cm^{-1} derived from calculated harmonic frequencies and intensities at the PBE0-D3(BJ)/def2-TZVP theory level. Relative energies are given in kcal mol^{-1}.

Vibrational assignment of the experimental infrared photodissociation spectrum of the [TaC_4O_8]$^+$ cation complex

The infrared photodissociation spectrum of the [TaC_4O_8]$^+$ cation shown in Fig. 5 was recorded in the range of 2200–2400 cm^{-1}, containing a spectral band centered at 2233 cm^{-1} and multiple absorptions covering a wide energy range with the most intense one at 2346 cm^{-1}. The band at

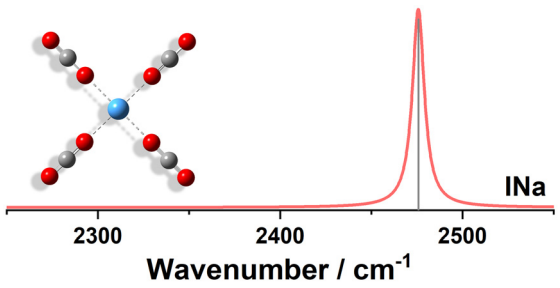

Fig. 4 Simulated vibrational spectrum of the lowest-energy isomer for the $[Ta(CO_2)_4]^+$ cation complex in the region of 2250–2550 cm^{-1} derived from calculated harmonic frequencies and intensities at the PBE0-D3(BJ)/def2-TZVP theory level.

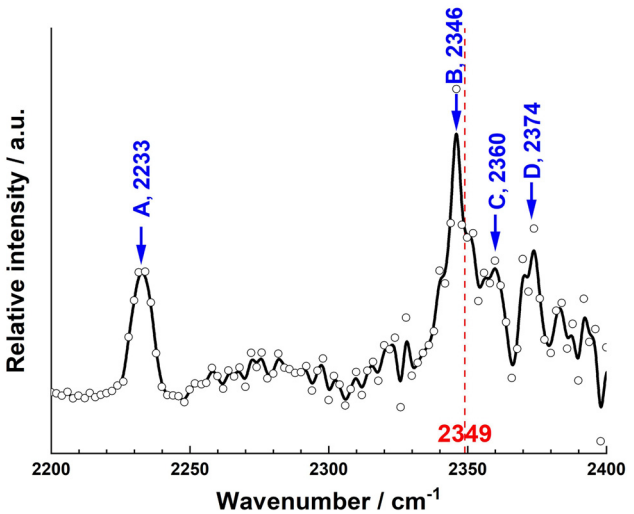

Fig. 5 Infrared photodissociation spectrum of the $[TaC_4O_8]^+$ cation complex in the spectral range of 2200–2400 cm^{-1}. Main vibrational peaks, A–D, are noted and the dashed line at 2349 cm^{-1} corresponds to the asymmetric stretching vibrational frequency of a free CO_2 molecule.[77]

2233 cm^{-1} denoted as peak A can be easily assigned to the contribution of carbonyl stretching vibration, which is blue-shifted by 90 cm^{-1} with respect to the experimental free CO stretching frequency at 2143 cm^{-1}.[76] The existence of this peak provides solid evidence for the insertion reaction into the C═O bond of CO_2 by the Ta^+ cation and the formation of an oxocarbonyl core structure.

In the wide band ranging from 2330 to 2387 cm^{-1}, a series of peaks at 2346 (peak B), 2360 (peak C) and 2374 (peak D) cm^{-1} are marked in Fig. 5. In comparison to peak A, all these peaks are undoubtedly attributed to the asymmetric stretching vibration of CO_2 molecules in different chemical environments. As demonstrated in previous studies of the reactions between CO_2 and atomic transition metals,[9,35,55,78] the systematic blue-shift of the CO_2 asymmetric stretching frequency usually indicates an "end-on" binding configuration which largely arises from charge–quadrupole electrostatic interactions between the metal atoms and CO_2 molecules. The slightly red-shifted peak at 2346 cm^{-1} in this work is unusual in the infrared studies of cationic metal–CO_2 complexes; however, such a small shift is insufficient to define a new coordination mode between the cation core and CO_2 ligands given the uncertainty of current measurement (>1 cm^{-1}). Nonetheless, the complicated pattern in Fig. 5 clearly implies the presence of more than one isomeric configuration for the $[TaC_4O_8]^+$ cation complex in current experiments.

Based on our calculations, low-energy products with bond-inserted binding motifs, IDa and IMb, as well as the terminally bound configuration INa are considered to be representative of each core structure coexisting in the experimental observations. Fig. 6 shows the comparison of their simulated infrared spectra with the experimental spectrum to identify possible contributors to the spectral features. Considering the approximations in electronic structure calculations with less than a relativistic full configuration interaction and the employed harmonic potential energy surfaces, a scaling factor is usually used for calculated vibrational frequencies to better match the experimental spectrum. In this case, this scaling

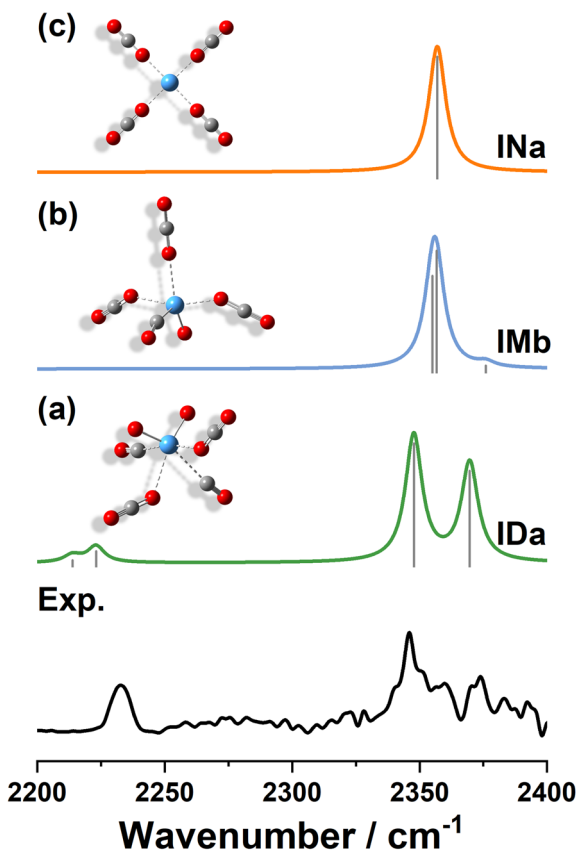

Fig. 6 Experimental and simulated vibrational spectra of the $[TaC_4O_8]^+$ cation complex in the spectral region of 2200–2400 cm^{-1}. The spectra (a–c) were simulated for the singlet IDa, the triplet IMb, and the quintet INa, with the calculated harmonic frequencies scaled by a factor of 0.952 and intensities at the PBE0-D3(BJ)/def2-TZVP level of theory.

factor was determined to be 0.957 or 0.956, respectively, by directly comparing the experimental and theoretical values of the free CO_2 asymmetric stretching vibrational frequencies[77] or the free CO stretching frequency.[76] However, the obtained vibrational frequencies are still higher than the experimental values, especially in the CO_2 asymmetric stretching vibrational frequency range. Therefore, a new scaling factor of 0.952 was artificially applied to achieve the best agreement between the experimental and simulated spectra.

In the CO stretching frequency range, only IDa among the three candidates has a broad vibrational band ranging from 2209 to 2230 cm^{-1} which matches well with peak A. Moreover, the relatively low frequency of CO stretch than the experimental value after scaling probably originates from the small scaling factor adopted here. Apart from peak A, two vibrational absorptions predicted at 2347 and 2370 cm^{-1} are in excellent agreement with peak B and D, in terms of both relative intensities and frequency values. According to the excellent agreement of both CO and CO_2 stretching frequency ranges, IDa is undoubtedly a competitive candidate for the observed $[TaC_4O_8]^+$ complex. This vibrational assignment corroborates the occurrence of oxygen-atom abstraction reactions between Ta^+ and CO_2 molecules, highlighting the critical role of spin crossover in the bond-insertion activation of CO_2 molecules. Noting that IDb also has two peaks with a similar spacing in the CO_2 asymmetric stretching frequency range as shown in Fig. 2b, its population can still be excluded from the main contributors based on the opposite order of the predicted spectral intensity to the experimental results.

For IMb with the $[TaO(CO)(CO_2)_3]^+$ structure, the carbonyl stretch locates out of the present experimental spectral range, making it difficult to conclusively confirm its existence. Encouragingly, the predominant band at 2356 cm^{-1} in the simulated IR spectrum of IMb perfectly reproduces peak C in Fig. 5 and a weak band at 2376 cm^{-1} can be faintly observed as well. Therefore, the contribution of IMb cannot be entirely ruled out to explain the complexity of this recorded spectrum. Furthermore, the predicted vibrational signatures of IMb and INa almost completely overlap in the CO_2 asymmetric stretching frequency range, providing no convincing evidence for the presence of isomer INa.

In summary, the overall spectral profile in the frequency range of 2200–2400 cm^{-1} can be well interpreted from the calculated infrared spectra of low-energy oxocarbonyl complexes, *i.e.* IDa and IMb, after vibrational frequency scaling. This finding reveals that starting from the initial encounter complex $^5[Ta\cdots OCO]^+$, the activation of CO_2 molecules by the Ta^+ cation occurs through insertion reactions into C═O bonds where two-state reactivity takes charge of this process.

Conclusion

In this work, the infrared photodissociation spectrum of the mass-selected cationic $[TaC_4O_8]^+$ complex in the 2200–2400 cm^{-1} region was measured and interpreted by comparison with DFT calculations. The appearance of an absorption at 2233 cm^{-1} in the carbonyl stretching frequency region indicates the occurrence of insertion reactions of the tantalum cation into the C═O bonds of CO_2. Vibrational assignment of the experimentally observed spectrum reveals the presence of two distinct inserted oxocarbonyl products in different spin states, *i.e.* the singlet $[TaO_2(CO)_2(CO_2)_2]^+$ and the triplet $[TaO(CO)(CO_2)_3]^+$ complex ions. Two-state reactivity plays a dictating role in driving successive insertion reactions and subsequent formation of metal–carbonyl complexes. The fundamental understanding of CO_2 activation by the tantalum cation provides a new perspective on the rational design of efficient catalysts for CO_2 reduction taking advantage of oxygen abstraction reactions.

Author contributions

J. H.: conceptualization, methodology, formal analysis, investigation and writing – original draft. P. L.: conceptualization and data curation. B. Q.: investigation and methodology. G. W., S. L. and X. Z.: supervision, writing – review & editing and funding acquisition.

Conflicts of interest

There are no conflicts of interest to declare.

Acknowledgements

This work was financially supported by the National Natural Science Foundation of China (No. 22073088, 21927805, and 21903079). X. Z. is also grateful for the support of the Fundamental Research Funds for the Central Universities. The quantum chemical calculations were performed on the supercomputing system in the Supercomputing Center of the University of Science and Technology of China.

References

1 H. Schwarz, *Coord. Chem. Rev.*, 2017, **334**, 112–123.
2 J. M. Weber, *Int. Rev. Phys. Chem.*, 2014, **33**, 489–519.
3 T. Zhang, W. P. Walawender, L. T. Fan, M. Fan, D. Daugaard and R. C. Brown, *J. Chem. Eng.*, 2004, **105**, 53–59.
4 Y. Wang, R. Kováčik, B. Meyer, K. Kotsis, D. Stodt, V. Staemmler, H. Qiu, F. Traeger, D. Langenberg, M. Muhler, *et al.*, *Angew. Chem., Int. Ed.*, 2007, **46**, 5624–5627.
5 L. Dietz, S. Piccinin and M. Maestri, *J. Phys. Chem. C*, 2015, **119**, 4959–4966.
6 S. Bontemps, L. Vendier and S. Sabo-Etienne, *J. Am. Chem. Soc.*, 2014, **136**, 4419–4425.

7 J. Han, Y. Yang, B. Qiu, P. Liu, X. Wu, G. Wang, S. Liu and X. Zhou, *Phys. Chem. Chem. Phys.*, 2023, **25**, 13198–13208.
8 G. K. Koyanagi and D. K. Bohme, *J. Phys. Chem. A*, 2006, **110**, 1232–1241.
9 A. Iskra, A. S. Gentleman, A. Kartouzian, M. J. Kent, A. P. Sharp and S. R. Mackenzie, *J. Phys. Chem. A*, 2017, **121**, 133–140.
10 D. Yang, X. T. Kong, H. J. Zheng, M. Z. Su, Z. Zhao, H. Xie, H. J. Fan, W. Q. Zhang and L. Jiang, *J. Phys. Chem. A*, 2019, **123**, 3703–3708.
11 E. Barwa, T. F. Pascher, M. Oncak, C. van der Linde and M. K. Beyer, *Angew. Chem., Int. Ed.*, 2020, **59**, 7467–7471.
12 X. Liu, X. P. Xing, J. Zhao and X. F. Wang, *J. Phys. Chem. A*, 2015, **119**, 610–619.
13 J. Ma, T. T. Wang, J. J. Yang, J. Hu and X. P. Xing, *Phys. Chem. Chem. Phys.*, 2020, **22**, 25227–25235.
14 A. Yanagimachi, K. Koyasu, D. Y. Valdivielso, S. Gewinner, W. Schöllkopf, A. Fielicke and T. Tsukuda, *J. Phys. Chem. C*, 2016, **120**, 14209–14215.
15 A. E. Green, J. Justen, W. Schöllkopf, A. S. Gentleman, A. Fielicke and S. R. Mackenzie, *Angew. Chem., Int. Ed.*, 2018, **57**, 14822–14826.
16 D. Yang, X. Kong, H. Zheng, M. Su, Z. Zhao, H. Xie, H. Fan, W. Zhang and L. Jiang, *J. Phys. Chem. A*, 2019, **123**, 3703–3708.
17 O. V. Lushchikova, M. Szalay, T. Höltzl and J. M. Bakker, *Faraday Discuss.*, 2023, **242**, 252–268.
18 X.-Y. He, Y.-Z. Liu, J.-J. Chen, X. Lan, X.-N. Li and S.-G. He, *J. Phys. Chem. Lett.*, 2023, **14**, 6948–6955.
19 M. Sodupe, V. Branchadell, M. Rosi and C. W. Bauschlicher, *J. Phys. Chem. A*, 1997, **101**, 7854–7859.
20 T. Fan, X. H. Chen and Z. Y. Lin, *Chem. Commun.*, 2012, **48**, 10808–10828.
21 Y. H. Sun, X. L. Sun and X. R. Huang, *J. Phys. Chem. A*, 2018, **122**, 5848–5860.
22 D. García-López, L. Pavlovic and K. H. Hopmann, *Organometallics*, 2020, **39**, 1339–1347.
23 G. L. Gutsev, K. M. Tibbetts, L. G. Gutsev, S. M. Aldoshin and B. R. Ramachandran, *ChemPhysChem*, 2022, **23**, e202200277.
24 B. J. Knurr and J. M. Weber, *J. Am. Chem. Soc.*, 2012, **134**, 18804–18808.
25 B. J. Knurr and J. M. Weber, *J. Phys. Chem. A*, 2013, **117**, 10764–10771.
26 B. J. Knurr and J. M. Weber, *J. Phys. Chem. A*, 2014, **118**, 4056–4062.
27 B. J. Knurr and J. M. Weber, *J. Phys. Chem. A*, 2014, **118**, 8753–8757.
28 B. J. Knurr and J. M. Weber, *J. Phys. Chem. A*, 2014, **118**, 10246–10251.
29 L. G. Dodson, M. C. Thompson and J. M. Weber, *J. Phys. Chem. A*, 2018, **122**, 2983–2991.
30 M. C. Thompson, L. G. Dodson and J. M. Weber, *J. Phys. Chem. A*, 2017, **121**, 4132–4138.
31 G. Gregoire, J. Velasquez and M. A. Duncan, *Chem. Phys. Lett.*, 2001, **349**, 451–457.
32 R. S. Walters, N. R. Brinkmann, H. F. Schaefer and M. A. Duncan, *J. Phys. Chem. A*, 2003, **107**, 7396–7405.
33 G. Gregoire, N. R. Brinkmann, D. van Heijnsbergen, H. F. Schaefer and M. A. Duncan, *J. Phys. Chem. A*, 2003, **107**, 218–227.
34 N. R. Walker, R. S. Walters, G. A. Grieves and M. A. Duncan, *J. Chem. Phys.*, 2004, **121**, 10498–10507.
35 A. M. Ricks, A. D. Brathwaite and M. A. Duncan, *J. Phys. Chem. A*, 2013, **117**, 11490–11498.
36 E. I. Brewer, A. E. Green, A. S. Gentleman, P. W. Beardsmore, P. A. J. Pearcy, G. Meizyte, J. Pickering and S. R. Mackenzie, *Phys. Chem. Chem. Phys.*, 2022, **24**, 22716–22723.
37 X. P. Xing, G. J. Wang, C. X. Wang and M. F. Zhou, *Chin. J. Chem. Phys.*, 2013, **26**, 687–693.
38 G. J. Wang, C. X. Chi, J. M. Cui, X. P. Xing and M. F. Zhou, *J. Phys. Chem. A*, 2012, **116**, 2484–2489.
39 G. J. Wang, C. X. Chi, X. P. Xing, C. F. Ding and M. F. Zhou, *Sci. China: Chem.*, 2014, **57**, 172–177.
40 T. Lu, *Molclus program, 1.9.9*; **https://www.keinsci.com/research/molclus.html** (accessed 16/11/2020).
41 C. Bannwarth, S. Ehlert and S. Grimme, *J. Chem. Theory Comput.*, 2019, **15**, 1652–1671.
42 S. Grimme, C. Bannwarth and P. Shushkov, *J. Chem. Theory Comput.*, 2017, **13**, 1989–2009.
43 T. Lu and F. W. Chen, *J. Comput. Chem.*, 2012, **33**, 580–592.
44 C. Adamo and V. Barone, *J. Chem. Phys.*, 1999, **110**, 6158–6170.
45 S. Grimme, S. Ehrlich and L. Goerigk, *J. Comput. Chem.*, 2011, **32**, 1456–1465.
46 F. Weigend and R. Ahlrichs, *Phys. Chem. Chem. Phys.*, 2005, **7**, 3297–3305.
47 K. Fukui, *J. Phys. Chem.*, 1970, **74**, 4161–4163.
48 D. G. Truhlar and M. S. Gordon, *Science*, 1990, **249**, 491–498.
49 K. Fukui, *Acc. Chem. Res.*, 1981, **14**, 363–368.
50 C. Gonzalez and H. B. Schlegel, *J. Phys. Chem.*, 1990, **94**, 5523–5527.
51 M. J. Frisch, G. W. Trucks, H. B. Schlegel, G. E. Scuseria, M. A. Robb, J. R. Cheeseman, G. Scalmani, V. Barone, G. A. Petersson, H. Nakatsuji, *et al.*, *Gaussian 16, Rev. C.01*, Gaussian, Inc., Wallingford, CT, 2016.
52 R. Wesendrup and H. Schwarz, *Angew. Chem., Int. Ed. Engl.*, 1995, **34**, 2033–2035.
53 A. Iskra, A. S. Gentleman, E. M. Cunningham and S. R. Mackenzie, *Int. J. Mass Spectrom.*, 2019, **435**, 93–100.
54 M. F. Zhou and L. Andrews, *J. Phys. Chem. A*, 1998, **102**, 8251–8260.
55 N. R. Walker, R. S. Walters and M. A. Duncan, *J. Chem. Phys.*, 2004, **120**, 10037–10045.
56 N. R. Walker, R. S. Walters and M. A. Duncan, *New J. Chem.*, 2005, **29**, 1495–1503.
57 N. Walker, R. Walters, E. Pillai and M. Duncan, *J. Chem. Phys.*, 2003, **119**, 10471–10474.
58 N. Walker, R. Walters, M.-K. Tsai, K. Jordan and M. Duncan, *J. Phys. Chem. A*, 2005, **109**, 7057–7067.
59 S. Shaik, D. Danovich, A. Fiedler, D. Schroder and H. Schwarz, *Helv. Chim. Acta*, 1995, **78**, 1393–1407.

60 S. Shaik, *Int. J. Mass Spectrom.*, 2013, **354**, 5–14.
61 P. B. Armentrout, *Science*, 1991, **251**, 175–179.
62 S. Shaik, M. Filatov, D. Schroder and H. Schwarz, *Chem. – Eur. J.*, 1998, **4**, 193–199.
63 H. Schwarz, *Int. J. Mass Spectrom.*, 2004, **237**, 75–105.
64 D. Schroder, S. Shaik and H. Schwarz, *Acc. Chem. Res.*, 2000, **33**, 139–145.
65 B. C. Sweeny, S. G. Ard, N. S. Shuman and A. A. Viggiano, *J. Phys. Chem. A*, 2018, **122**, 4246–4251.
66 V. Canale, R. Robinson, A. Zavras, G. N. Khairallah, N. d'Alessandro, B. F. Yates and R. A. J. O'Hair, *J. Phys. Chem. Lett.*, 2016, **7**, 1934–1938.
67 S. D. Zhou, J. L. Li, M. Firouzbakht, M. Schlangen and H. Schwarz, *J. Am. Chem. Soc.*, 2017, **139**, 6169–6176.
68 A. K. Hickey, S. A. Lutz, C. H. Chen and J. M. Smith, *Chem. Commun.*, 2017, **53**, 1245–1248.
69 Y. H. Sun, H. Tang, K. J. Chen, L. R. Hu, J. N. Yao, S. Shaik and H. Chen, *J. Am. Chem. Soc.*, 2016, **138**, 3715–3730.
70 A. J. Lupinetti, G. Frenking and S. H. Strauss, *Angew. Chem., Int. Ed.*, 1998, **37**, 2113–2116.
71 A. D. Brathwaite, A. M. Ricks and M. A. Duncan, *J. Phys. Chem. A*, 2013, **117**, 13435–13442.
72 G. Bistoni, S. Rampino, N. Scafuri, G. Ciancaleoni, D. Zuccaccia, L. Belpassi and F. Tarantelli, *Chem. Sci.*, 2016, **7**, 1174–1184.
73 G. Ciancaleoni, L. Belpassi and F. Marchetti, *Inorg. Chem.*, 2017, **56**, 11266–11274.
74 S. C. C. van der Lubbe, P. Vermeeren, C. Fonseca Guerra and F. M. Bickelhaupt, *Chem. – Eur. J.*, 2020, **26**, 15690–15699.
75 G. Frenking, I. Fernández, N. Holzmann, S. Pan, I. Krossing and M. Zhou, *JACS Au*, 2021, **1**, 623–645.
76 K.-P. Huber, *Molecular spectra and molecular structure: IV. Constants of diatomic molecules*, Springer Science & Business Media, 2013.
77 G. Herzberg, *Molecular spectra and molecular structure*, D. van Nostrand, 1945.
78 Z. Zhao, X. T. Kong, D. Yang, Q. Q. Yuan, H. Xie, H. J. Fan, J. J. Zhao and L. Jiang, *J. Phys. Chem. A*, 2017, **121**, 3220–3226.